Journal of Quantitative Spectroscopy & Radiative Transfer 189 (2017) 112–125

Contents lists available at ScienceDirect

Journal of Quantitative Spectroscopy & Radiative Transfer

journal homepage: www.elsevier.com/locate/jqsrt

Physical explanation of the SLIPI technique by the large scatterer approximation of the RTE

Elias Kristensson [a], Gerhard Kristensson [b,*]

[a] Department of Physics, Division of Combustion Physics, Lund University, P.O. Box 118, SE-221 00 Lund, Sweden
[b] Department of Electrical and Information Technology, Lund University, P.O. Box 118, SE-221 00 Lund, Sweden

ARTICLE INFO

Article history:
Received 11 October 2016
Received in revised form
21 November 2016
Accepted 21 November 2016

Keywords:
Multiple light scattering suppression
Imaging in turbid media
Structured illumination
Radiative transfer equation
Large scatterer approximation

ABSTRACT

Visualizing the interior of a turbid scattering media by means light-based methods is not a straightforward task because of multiple light scattering, which generates image blur. To overcome this issue, a technique called Structured Laser Illumination Planar Imaging (SLIPI) was developed within the field of spray imaging. The method is based on a 'light coding' strategy to distinguish between directly and multiply scattered light, allowing the intensity from the latter to be suppressed by means of data post-processing. Recently, the performance of the SLIPI technique was investigated, during which deviations from theoretical predictions were discovered. In this paper, we aim to explain the origin of these deviations, and to achieve this end, we have performed several SLIPI measurements under well-controlled conditions. Our experimental results are compared with a theoretical model that is based on the large scatterer approximation of the Radiative Transfer Equation but modified according to certain constraints. Specifically, our model is designed to (1) ignore all off-axis intensity contributions, (2) to treat unperturbed- and forward-scattered light equally and (3) to accept light to scatter within a narrow forward-cone as we believe these are the rules governing the SLIPI technique. The comparison conclusively shows that optical measurements based on scattering and/or attenuation in turbid media can be subject to significant errors if not all aspects of light-matter interactions are considered. Our results indicate, as were expected, that forward-scattering can lead to deviations between experiments and theoretical predictions, especially when probing relatively large particles. Yet, the model also suggests that the spatial frequency of the superimposed 'light code' as well as the spreading of the light-probe are important factors one also needs to consider. The observed deviations from theoretical predictions could, however, potentially be exploited to assess particle size.

1. Introduction

Structured Laser Illumination Planar Imaging (SLIPI) is an optical imaging technique primarily used to visualize spray-related phenomena, such as the disintegration of liquid into fine, spherical droplets [1,2]. SLIPI is based on (1) laser sheet imaging [3], where a laser beam is formed into a thin sheet of light and (2) structured illumination [4], which employs an intensity modulation scheme to permit added post-processing possibilities. The purpose of a laser sheet is to illuminate only a single plane of the sample, *i.e.*, to optically select a "slice" of the sample. A camera positioned at a 90 degrees angle records the signal that is generated by the laser sheet, resulting in a 2D view of the illuminated sample.

The laser sheet technique has been widely used in several fields, such as combustion research, biology and fluid dynamics [3,5,6]. However, when the method is applied to optically dense, highly scattering environments, the electromagnetic field interacts in a complex way with the entire medium — not only with the droplets in the laser sheet, but also with the ones outside. Multiple scattering effects dominates in this situation. As the laser sheet method assumes singly scattered light only, the detection of multiply scattered light causes measurement errors such as a reduced image contrast, concealment of structures and incorrect intensity levels [1,2,7]. To address this issue, laser sheet imaging can be combined with the structured illumination method — a unification named SLIPI. With SLIPI, the laser beam is guided through a transmission Ronchi grating, which adds a sinusoidal line structure to the otherwise homogeneous intensity profile of the laser sheet. The line structure has one primary purpose: providing means to differentiate between light that has been repeatedly scattered within the sample and light that has only interacted with the sample once. Only light that is directly scattered from the laser sheet to the detector is guaranteed to preserve this

* Corresponding author.
E-mail addresses: Elias.Kristensson@forbrf.lth.se (E. Kristensson), Gerhard.Kristensson@eit.lth.se (G. Kristensson).

http://dx.doi.org/10.1016/j.jqsrt.2016.11.019
0022-4073/

superimposed line structure in the detected image, whereas light that has been scattered several times lose this structural information due to random averaging. By post-processing the acquired data, the latter unwanted contribution can be greatly suppressed, leading to improved visualization of turbid, scattering objects.

In an attempt to better understand the potential and limitations of the SLIPI technique, Kristensson and coworkers performed measurements on several cuvettes with a homogeneous mixture of water and polystyrene spheres, which both scattered and absorbed light [8]. Number density and particle size were altered in a controlled fashion, which allowed them to compare the results with the Bouguer-Beer law.[1] It was discovered that the SLIPI technique did not produce results in complete agreement with this well-known law. In particular, an increased particle size resulted in larger deviations from theoretical predictions, a trend that the authors attributed to differences in the scattering phase function of the particles. In the size-range 1 to 30 μm, larger particles have a pronounced forward scattering lobe that grows in magnitude with size. This implies that the light intensity is enhanced in the forward direction — the more the larger the particle. Since light that does not deviate from its initial trajectory will preserve the line structure employed in SLIPI, it cannot be suppressed with the technique, thus resulting in the observed deviations from the Bouguer-Beer law. Fig. 1 illustrates this forward-scattering lobe structure for three different particle sizes.

In this paper, we intend to investigate the accuracy of this proposed explanation. To achieve this end and thereby better understand the physics governing light-matter interactions in general and the SLIPI technique in particular, we have performed SLIPI measurements under well-controlled conditions. The results are compared with theoretical prediction based on a solution of the Radiative Transfer Equation (RTE) using the large scatterer approximation.

2. Experimental arrangements

2.1. SLIPI optical setup

A schematic of the experimental setup is presented in Fig. 2. The laser light ($\lambda = 447$ nm) was first expanded using a telescope of two lenses and then guided through an aperture to select the central region. The light was then guided through a Ronchi transmission grating, which diffracts the laser light, and a cylindrical lens focused the interference orders onto a so-called 'frequency cutter'. The purpose of this device was to physically block all but the two fundamental orders. As these two identically intense beams overlapped, they created, by interference, a sinusoidally modulated intensity profile. A second cylindrical lens was then used to focus the modulated light into a thin sheet of light (≈ 100 μm). A second telescope arrangement (cylindrical lenses) was used to alter the frequency of the intensity modulation. A sensitive EM-CCD (Andor Luca), mounted at a 90 degrees angle, was used to collect the signal from the laser sheet.

The purpose of the modulation scheme is, as mentioned above, to differentiate between the intensity contributions originating from singly and multiply scattered light. Light, that is repeatedly scattered within the sample, tends to loose the modulation feature that is encoded into the illumination, whereas directly (singly) scattered light remains faithful to this spatial structure. If the phase of the modulation structure is slightly altered, the spatial distribution of the directly scattered light shifts accordingly, while the intensity contribution stemming from multiply scattered light remains unaffected. By calculating the pixel-wise root-mean-square (RMS) between three so-called subimages having spatial phases of 0, $2\pi/3$ and $4\pi/3$ the modulated component — the singly scattered light — is extracted, and the DC-component — the multiply scattered light — is suppressed [1]. An example of the process is given in Fig. 3.

The SLIPI concept can be also understood in terms of spatial frequencies. All signals of interest are modulated by a well-defined spatial frequency, while unwanted background features are characterized by other (not necessarily low) spatial frequencies. Calculating the pixel-wise RMS between the three subimages corresponds to extracting the image information modulated by the spatial frequency of the laser sheet.

2.2. Sample preparation

Six suspensions of water and non-absorbing microspheres were used in the experiments, having approximate diameters of 4.5, 6, 10, 15, 20, and 25 μm, respectively. These particles were assumed to be spherical. All mixtures were prepared to have an optical depth of $OD = 2$, where optical depth is defined as the sample length (44 mm) multiplied by the average extinction coefficient (number density or concentration times the extinction cross section σ_{ext}), in this case corresponding to a value of 0.045 mm^{-1}. The particles were delivered in 5 ml containers, with the total number of particles specified in each batch. By knowing the extinction cross sections (σ_{ext}) for the particles, the required number density corresponding to the desired average extinction could be calculated, see Table 1. Each sample was prepared according to the following procedure:

1. An empty 2 liters bottle was placed on a scale with milligram precision and its weight was noted.
2. The particles were emptied into to the bottle and the container carefully rinsed. The weight of the particles was neglected.
3. The amount of water specified in Table 1 was added to the bottle using the scale to monitor the added volume. Since the amount of water needed in each case differed, the precision of the mixing process varied slightly.
4. 100 ml of the mixture was poured into a glass cuvette ($44 \times 34 \times 100$ mm^3).
5. To avoid particles sticking onto the glass surfaces, the cuvette was placed in an ultrasonic cleaner prior to the measurement.

2.3. Measurement scheme

Although the purpose of the investigation was to understand how differences in the Mie scattering phase function affected the outcome of a SLIPI measurement, direct comparison with the *scattered* light had to be avoided for experimental reasons. When visualizing the Mie scattered light from a spatially homogeneous sample of identical particle size, even minute changes in the collection- and acceptance angle affect the resulting image because of the rapid angular variations in the Mie scattering phase function. Comparing the experimental data with the theoretical model would, in such a case, require the exact knowledge of the angle between laser sheet and the detector as well as the acceptance angles, which are both difficult to assess with sufficiently high precision. Fig. 4 shows plots extracted from Mie scattering images of the mixtures, where the influence of the lobe structures are noticeable.

To circumvent the issue with the side-scattering lobes experimentally, a small amount of fluorescing dye was added to each

[1] Also known as Beer's law, the Beer-Lambert law, the Lambert-Beer law, or the Beer-Lambert-Bouguer law *etc.*, but it is incorrect to accredit Lambert to this law, since Bouguer made the original contributions [9]. For a comprehensive survey of the history of the law see [10].

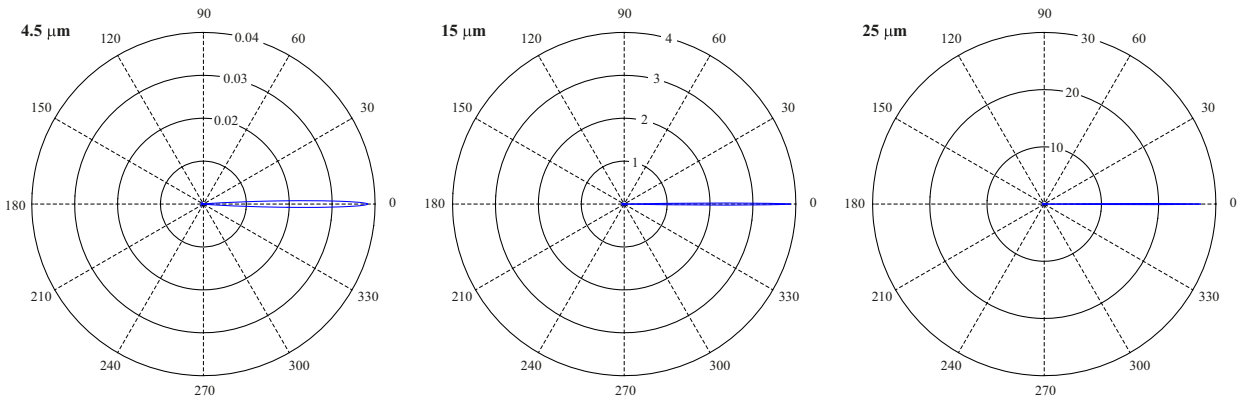

Fig. 1. Mie scattering phase functions for three different particle sizes (λ = 447 nm), shown in a *linear* scale. The (unconventional) linear representation of the scattering phase functions illustrates the strong forward-scattering phenomenon — the stronger the larger the particle.

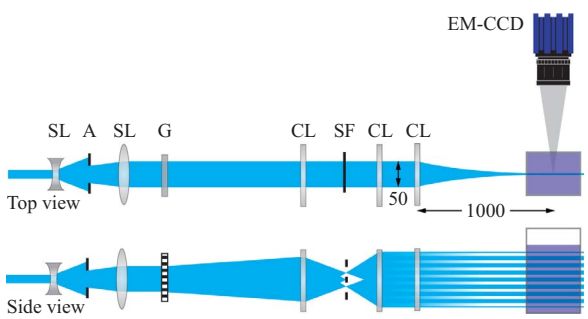

Fig. 2. The experimental setup. SL=Spherical Lens. A=Aperture. G=Grating. CL=Cylinder Lens. SF=Spatial Filter.

mixture. Since the inelastic fluorescence signal (LIF) is nearly isotopic and identical for all mixtures under study, the exact position of the camera with respect to the laser sheet is no longer a critical factor. By compensating for the loss of light introduced by the added dye ($OD \approx 0.1$), the approach thus allowed monitoring of the relative loss of light intensity as a function of distance, without being influenced by the specifics of the detection system. Fig. 5 illustrates this procedure.

The refractive index of the spheres immersed in water is determined by [11]

$$n(\lambda) = A + \frac{B}{\lambda^2} + \frac{C}{\lambda^4}$$

where, if λ is the wavelength in vacuum measured in nm, the constants $A=1.5725$, $B=3108.0$, and $C = 34779 \cdot 10^4$, resulting in a refractive index of $m=1.60$ at $\lambda = 447$ nm.

3. Theory

The quantitative modeling of the SLIPI experiment is now addressed in detail. The aim of the theoretical model is to understand and explain the results of the SLIPI experiments, both qualitatively and quantitatively. To achieve this end, the model needs to accurately model the signal generated in a SLIPI measurement. The two main challenges of this task are: (1) the signal is generated by a laser *sheet* and (2) light contributions from other directions than in a neighborhood of the forward direction must be neglected (as these are suppressed with the SLIPI technique). Indeed, the theoretical model presented in this section corroborates all essential details of the experimental results and can, in fact, be used to design future experiments.

The radiative transfer equation (RTE) [12,13] is commonly adopted as a model for computations of the intensity variations in

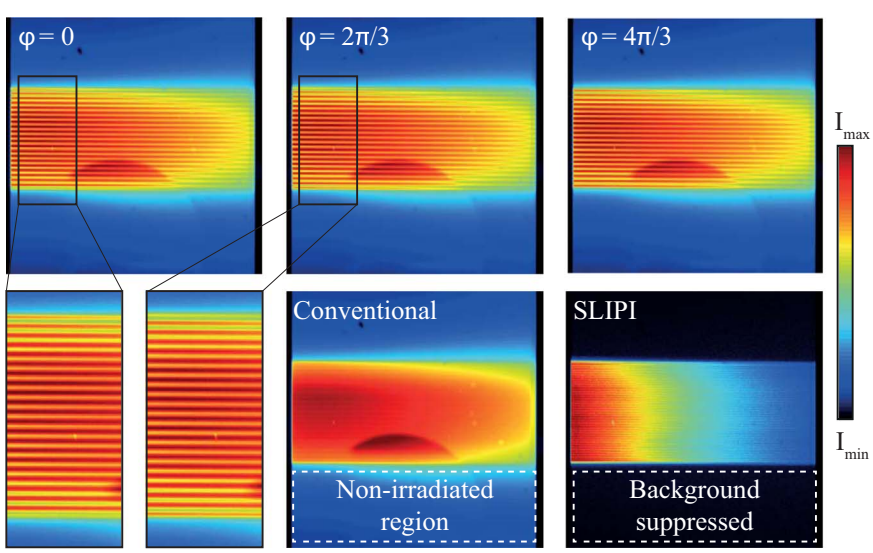

Fig. 3. The SLIPI process, illustrated on one of the cuvettes used in the current study. To suppress the contribution from multiply scattered light (and other signal interferences), three so-called subimages are recorded, between which the spatial phase is altered 1/3 of the superimposed sinusoidal period. The "conventional" image shows the laser sheet signal without any suppression of the multiply scattered light, where unwanted signal stemming from non-irradiated regions of the sample can be observed. Such interferences are efficiently removed using the SLIPI data post-processing.

Table 1
Sample-related characteristics. N corresponds to the total number of particles in a 5 ml bottle, σ_{ext} is the extinction cross section, H_2O is the amount of water needed to achieve the desired concentration, C, that gives an OD of 2 over 44 mm. The explicit diameters delivered by the manufacturer were: 4.518, 5.94, 11.00, 15.66, 18.79, 24.90 μm, respectively.

Size [μm]	4.5	6	10	15	20	25
N	2.495×10^9	1.05×10^9	2.275×10^8	6.75×10^8	2.84×10^7	1.455×10^7
σ_{ext} [μm^2]	35.0	60.9	208	407	571	984
H_2O [ml]	1986.46	1376.15	831.506	561.564	411.594	321.192
C [mm^{-3}]	1330	807	218	109	85.7	47.7

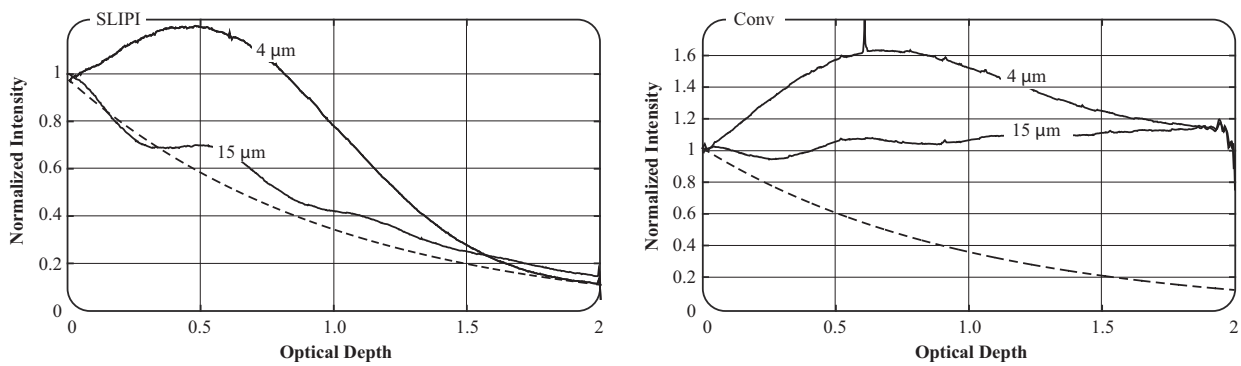

Fig. 4. Cross-sections from two images where only Mie scattered light was collected, together with the decay of light intensity as predicted by the Bouguer-Beer law (dashed line). Both SLIPI and conventional data clearly show how the influence of the Mie scattering lobes makes any theoretical comparison challenging.

random media. The problem addressed in this paper requires the use of a 3D RTE for a homogeneous medium to obtain a correct model for the intensity. This is a consequence of the inhomogeneous illumination by the laser sheet. The RTE quantifies the intensity $I(\boldsymbol{r}, \hat{\boldsymbol{n}})$ at a point $\boldsymbol{r}$ in the medium in a specific direction $\hat{\boldsymbol{n}}$. The effect of the polarization state of the intensity is ignored in the scalar version of RTE. A vector formulation of RTE is available, which also quantifies the polarization effects by an employment of the Stokes parameters [14,15]. However, the experimental results in this paper have very little polarization information, and, therefore, the scalar version of RTE suffices. Moreover, the RTE holds for sparse suspensions, which is assumed to hold for the samples prepared in this paper.

The RTE has no closed form solutions for the conditions considered in this paper, and numerical techniques have to be employed. However, in several situations approximations apply, which lead to closed form solutions of great value. One such approximation is the assumption of electrically large scatterers in the medium. In the results presented in this paper, the scatterers are electrically large, $ka \approx [30, 165]$, where k is the wave number of the microspheres relative to the background material in the cuvette [11], and a is the radius of the spheres. In this section, a review of the approximation employed in this paper is presented.

Alternative approaches to solve the present problem exist, see *e.g.*, [16] and the discussion therein.

3.1. The radiative transport equation

There are two main assumptions made in this paper, which dramatically simplify the solution of the RTE: (1) the homogeneity assumption, *i.e.*, σ_{ext} and σ_{sc} do not depend on location or directions — only on frequency, and (2) the forward scattering assumption, which is explained below.

The pertinent scalar version of the radiative transfer equation (RTE), or transport equation, for the intensity $I(\boldsymbol{r}, \hat{\boldsymbol{n}})$ at the position $\boldsymbol{r}$ in the direction $\hat{\boldsymbol{n}}$ for a homogeneous suspension is, see *e.g.*, [13, Ch. 7 & 11] and [14, Eq. (8.11.5)]

$$\hat{\boldsymbol{n}}\cdot\nabla I(\boldsymbol{r}, \hat{\boldsymbol{n}}) = -n_0\sigma_{\text{ext}}(\hat{\boldsymbol{n}})I(\boldsymbol{r}, \hat{\boldsymbol{n}}) + \frac{n_0}{4\pi}\iint_{\Omega}\frac{\mathrm{d}\sigma}{\mathrm{d}\Omega}(\hat{\boldsymbol{n}}, \hat{\boldsymbol{n}}')I(\boldsymbol{r}, \hat{\boldsymbol{n}}')\mathrm{d}\Omega'$$

where Ω denotes the unit sphere, n_0 the number density (number of scatterers per unit volume), $\sigma_{\text{ext}}(\hat{\boldsymbol{n}})$ the extinction cross section (incidence in the $\hat{\boldsymbol{n}}$ direction), and where $\frac{\mathrm{d}\sigma}{\mathrm{d}\Omega}(\hat{\boldsymbol{n}}, \hat{\boldsymbol{n}}')$ denotes the differential scattering cross section of the single scatterer in the direction $\hat{\boldsymbol{n}}$ (incident direction $\hat{\boldsymbol{n}}'$). The scattering cross section $\sigma_s(\hat{\boldsymbol{n}})$ is [17]

$$\sigma_s(\hat{\boldsymbol{n}}) = \frac{1}{4\pi}\iint_{\Omega}\frac{\mathrm{d}\sigma}{\mathrm{d}\Omega}(\hat{\boldsymbol{n}}', \hat{\boldsymbol{n}})\mathrm{d}\Omega'$$

Introduce the phase function $p(\hat{\boldsymbol{n}}, \hat{\boldsymbol{n}}')$ defined as[2]

$$p(\hat{\boldsymbol{n}}, \hat{\boldsymbol{n}}') = \frac{1}{4\pi\sigma_{\text{ext}}(\hat{\boldsymbol{n}}')}\frac{\mathrm{d}\sigma}{\mathrm{d}\Omega}(\hat{\boldsymbol{n}}, \hat{\boldsymbol{n}}')$$

with normalization

$$\iint_{\Omega} p(\hat{\boldsymbol{n}}', \hat{\boldsymbol{n}})\mathrm{d}\Omega' = \frac{\sigma_s(\hat{\boldsymbol{n}})}{\sigma_{\text{ext}}(\hat{\boldsymbol{n}})} = \alpha(\hat{\boldsymbol{n}})$$

where $\alpha(\hat{\boldsymbol{n}})$ denotes the single scatterer albedo.

For spherical objects, the phase function depends only on the difference between the directions $\hat{\boldsymbol{n}}$ and $\hat{\boldsymbol{n}}'$ (more precisely, the absolute value of the difference,[3] $|\hat{\boldsymbol{n}} - \hat{\boldsymbol{n}}'|$). The phase function for a homogeneous material of spherical scatterers then has the form

$$p(\hat{\boldsymbol{n}} - \hat{\boldsymbol{n}}') = \frac{1}{4\pi\sigma_{\text{ext}}}\frac{\mathrm{d}\sigma}{\mathrm{d}\Omega}(\hat{\boldsymbol{n}} - \hat{\boldsymbol{n}}')$$

and the RTE simplifies to

$$\hat{\boldsymbol{n}}\cdot\nabla I(\boldsymbol{r}, \hat{\boldsymbol{n}}) = -n_0\sigma_{\text{ext}}I(\boldsymbol{r}, \hat{\boldsymbol{n}}) + n_0\sigma_{\text{ext}}\iint_{\Omega} p(\hat{\boldsymbol{n}} - \hat{\boldsymbol{n}}')I(\boldsymbol{r}, \hat{\boldsymbol{n}}')\mathrm{d}\Omega'$$

or if all distances are measured in units of the optical distance, OD ($\boldsymbol{r}_{\text{OD}} = \boldsymbol{r}n_0\sigma_{\text{ext}}$)

[2] Other definitions occur — a factor of 4π differs and occasionally the scattering cross section is used instead of the extinction cross section.

[3] The independent variable is $\cos\theta = \hat{\boldsymbol{n}}\cdot\hat{\boldsymbol{n}}' = 1 - |\hat{\boldsymbol{n}} - \hat{\boldsymbol{n}}'|^2/2$.

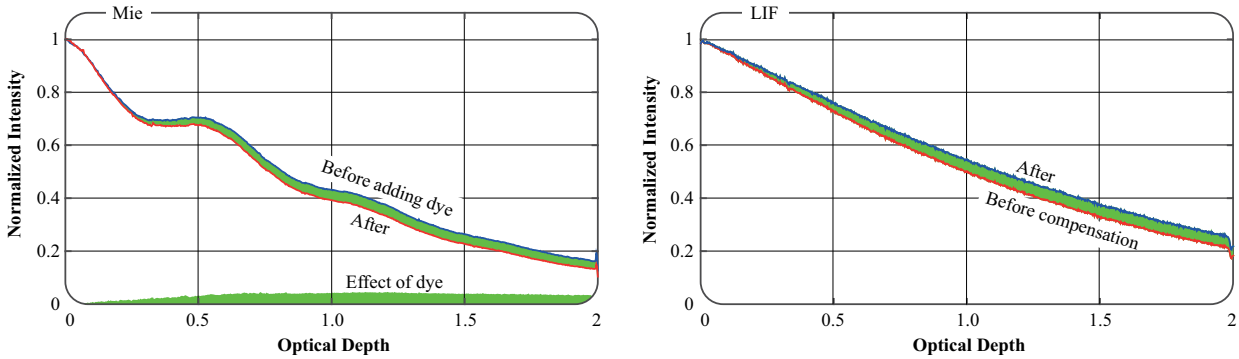

Fig. 5. To avoid measurement uncertainties caused by the lobe structure of the scattering phase function, a small amount of fluorescing dye was added to the cuvette. SLIPI measurements were carried out both prior to and after the dye was added, thus permitting us to assess the slightly increased *OD* (left panel). As the dye emitted light (LIF) nearly isotropically, the local light intensity *within* the cuvette could be monitored. However, since only the loss of energy caused by scattering was of interest, the added opacity of the dye was compensated for (right panel).

$$\hat{\boldsymbol{n}}\cdot\nabla_{\mathrm{OD}}\, I(\boldsymbol{r}_{\mathrm{OD}}, \hat{\boldsymbol{n}}) = -I(\boldsymbol{r}_{\mathrm{OD}}, \hat{\boldsymbol{n}}) + \iint_{\Omega} p(\hat{\boldsymbol{n}} - \hat{\boldsymbol{n}}')I(\boldsymbol{r}_{\mathrm{OD}}, \hat{\boldsymbol{n}}')\mathrm{d}\Omega' \tag{3.1}$$

4. Large scatterer approximation

The slab geometry of interest in this paper is depicted in Fig. 6. The spheres are suspended in water between $0 \le z \le d$ or in terms of the scaled variables, $\tau = n_0\sigma_{\mathrm{ext}}z$, between $0 \le \tau \le \tau_0 = n_0\sigma_{\mathrm{ext}}d$. The scaled lateral variables are denoted $\boldsymbol{\eta} = n_0\sigma_{\mathrm{ext}}(x\hat{\boldsymbol{x}} + y\hat{\boldsymbol{y}})$.

The analysis reviewed in this section follows Ishimaru closely [13, Chapter 13] and [18]. An electrically large object scatters strongly in the forward direction, and less in all other directions, see Fig. 1. This fact motivates the large scatterer approximation, which neglects all scattering contributions except for a cone in the forward direction.

The final goal is to compute the light intensity in a neighborhood of the forward direction $\hat{\boldsymbol{n}} = \hat{\boldsymbol{z}}$. The direction $\hat{\boldsymbol{n}} = s_x\hat{\boldsymbol{x}} + s_y\hat{\boldsymbol{y}} + s_z\hat{\boldsymbol{z}}$, expressed in Cartesian coordinates, is subject to the constraint $s_x^2 + s_y^2 + s_z^2 = 1$. Most of the variation in the intensity takes place in the forward direction $s_z \approx 1$, *i.e.*, the scattering angle is always small. Therefore, the directional derivative is approximated with

$$\hat{\boldsymbol{n}}\cdot\nabla_{\mathrm{OD}} = s_z\frac{\partial}{\partial\tau} + \boldsymbol{s}\cdot\nabla_{\mathrm{OD}} \approx \frac{\partial}{\partial\tau} + \boldsymbol{s}\cdot\nabla_{\mathrm{OD}}$$

In the integral over the unit sphere, the lateral variable $\boldsymbol{s} = s_x\hat{\boldsymbol{x}} + s_y\hat{\boldsymbol{y}}$ is restricted by $s_x^2 + s_y^2 \le 1$, but due to the vanishing contribution of the phase function when $s_x^2 + s_y^2 > 1$, the integration in $\boldsymbol{s}$ can be extended to the entire x-y plane, without a major change in the value of the integral.

As a consequence of the assumptions made above, the RTE in (3.1) is approximated by

$$\frac{\partial}{\partial\tau}I(\boldsymbol{\eta}, \tau, \boldsymbol{s}) + \boldsymbol{s}\cdot\nabla_{\mathrm{OD}}\, I(\boldsymbol{\eta}, \tau, \boldsymbol{s}) = -I(\boldsymbol{\eta}, \tau, \boldsymbol{s}) + \iint_{\mathbb{R}^2} p(\boldsymbol{s} - \boldsymbol{s}')I(\boldsymbol{\eta}, \tau, \boldsymbol{s}')\mathrm{d}\boldsymbol{s}'$$

where $\boldsymbol{s} = s_x\hat{\boldsymbol{x}} + s_y\hat{\boldsymbol{y}}$, $\boldsymbol{\eta} = n_0\sigma_{\mathrm{ext}}(x\hat{\boldsymbol{x}} + y\hat{\boldsymbol{y}})$, $\tau = n_0\sigma_{\mathrm{ext}}z$, and where the phase function is $p(\boldsymbol{s} - \boldsymbol{s}')$.[4] It is assumed that the phase function has its main contribution for small arguments $|\boldsymbol{s} - \boldsymbol{s}'|$.

[4] Holds as an approximation in the forward direction, and the phase function is assumed to depend only on $\boldsymbol{s} - \boldsymbol{s}'$ — in reality $|\hat{\boldsymbol{n}} - \hat{\boldsymbol{n}}'|^2 = |s_z\hat{\boldsymbol{z}} + \boldsymbol{s} - s_z{}'\hat{\boldsymbol{z}} - \boldsymbol{s}'|^2 = (s_z - s_z{}')^2 + |\boldsymbol{s} - \boldsymbol{s}'|^2 \approx |\boldsymbol{s} - \boldsymbol{s}'|^2$, since we eventually are going to evaluate the intensity in the forward direction.

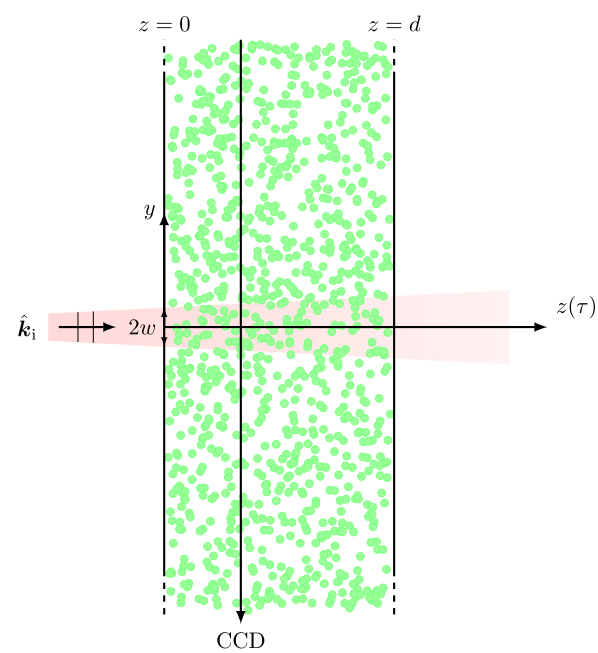

Fig. 6. The geometry of a slab illuminated with a beam (laser sheet) of limited extent as seen from above. The width of the laser sheet at $\tau = 0$ is $2w$, and the direction of the exterior excitation is $\hat{\boldsymbol{k}}_{\mathrm{i}}$ (normal incidence).

Proceed by a Fourier transform of the RTE w.r.t. to η. The result is

$$\frac{\mathrm{d}}{\mathrm{d}\tau}I(\boldsymbol{\kappa}, \tau, \boldsymbol{s}) = -(1 - \mathrm{i}\boldsymbol{s}\cdot\boldsymbol{\kappa})I(\boldsymbol{\kappa}, \tau, \boldsymbol{s}) + \iint_{\mathbb{R}^2} p(\boldsymbol{s} - \boldsymbol{s}')I(\boldsymbol{\kappa}, \tau, \boldsymbol{s}')\mathrm{d}\boldsymbol{s}'$$

where

$$I(\boldsymbol{\kappa}, \tau, \boldsymbol{s}) = \iint_{\mathbb{R}^2} I(\boldsymbol{\eta}, \tau, \boldsymbol{s})\mathrm{e}^{\mathrm{i}\boldsymbol{\kappa}\cdot\boldsymbol{\eta}}\,\mathrm{d}\boldsymbol{\eta}$$

with inverse

$$I(\boldsymbol{\eta}, \tau, \boldsymbol{s}) = \frac{1}{4\pi^2}\iint_{\mathbb{R}^2} I(\boldsymbol{\kappa}, \tau, \boldsymbol{s})\mathrm{e}^{-\mathrm{i}\boldsymbol{\kappa}\cdot\boldsymbol{\eta}}\,\mathrm{d}\boldsymbol{\kappa}$$

To avoid cumbersome notation in the analysis here and below, we use the same symbol for the Fourier transform of the intensity as for the intensity itself. The arguments distinguish the two quantities.

A simplified notation is introduced to facilitate the analysis.

$$I(\boldsymbol{\kappa}, \tau, \boldsymbol{s}) = F(\boldsymbol{\kappa}, \tau, \boldsymbol{s})\mathrm{e}^{-(1-\mathrm{i}\boldsymbol{s}\cdot\boldsymbol{\kappa})\tau}$$

where $F(\boldsymbol{\kappa}, \tau, \boldsymbol{s})$ satisfies

$$\frac{\mathrm{d}}{\mathrm{d}\tau}F(\boldsymbol{\kappa}, \tau, \boldsymbol{s}) = \iint_{\mathbb{R}^2} p(\boldsymbol{s}-\boldsymbol{s}')F(\boldsymbol{\kappa}, \tau, \boldsymbol{s}')\mathrm{e}^{-\mathrm{i}(\boldsymbol{s}-\boldsymbol{s}')\cdot\boldsymbol{\kappa}\tau}\,\mathrm{d}\boldsymbol{s}'$$

Now introduce the Fourier transform *w. r. t.* the variable $\boldsymbol{s}$. The following notation is used:

$$p(\boldsymbol{q}) = \iint_{\mathbb{R}^2} p(\boldsymbol{s})\mathrm{e}^{\mathrm{i}\boldsymbol{q}\cdot\boldsymbol{s}}\,\mathrm{d}\boldsymbol{s}$$

and

$$I(\boldsymbol{\kappa}, \tau, \boldsymbol{q}) = \iint_{\mathbb{R}^2} I(\boldsymbol{\kappa}, \tau, \boldsymbol{s})\mathrm{e}^{\mathrm{i}\boldsymbol{q}\cdot\boldsymbol{s}}\,\mathrm{d}\boldsymbol{s}, \quad F(\boldsymbol{\kappa}, \tau, \boldsymbol{q}) = \iint_{\mathbb{R}^2} F(\boldsymbol{\kappa}, \tau, \boldsymbol{s})\mathrm{e}^{\mathrm{i}\boldsymbol{q}\cdot\boldsymbol{s}}\,\mathrm{d}\boldsymbol{s}$$

with inverses

$$p(\boldsymbol{s}) = \frac{1}{4\pi^2}\iint_{\mathbb{R}^2} p(\boldsymbol{q})\mathrm{e}^{-\mathrm{i}\boldsymbol{q}\cdot\boldsymbol{s}}\,\mathrm{d}\boldsymbol{q}$$

and

$$I(\boldsymbol{\kappa}, \tau, \boldsymbol{s}) = \frac{1}{4\pi^2}\iint_{\mathbb{R}^2} I(\boldsymbol{\kappa}, \tau, \boldsymbol{q})\mathrm{e}^{-\mathrm{i}\boldsymbol{q}\cdot\boldsymbol{s}}\,\mathrm{d}\boldsymbol{q},$$
$$F(\boldsymbol{\kappa}, \tau, \boldsymbol{s}) = \frac{1}{4\pi^2}\iint_{\mathbb{R}^2} F(\boldsymbol{\kappa}, \tau, \boldsymbol{q})\mathrm{e}^{-\mathrm{i}\boldsymbol{q}\cdot\boldsymbol{s}}\,\mathrm{d}\boldsymbol{q}$$

Between the Fourier transforms of the intensity, $I(\boldsymbol{\kappa}, \tau, \boldsymbol{q})$, and $F(\boldsymbol{\kappa}, \tau, \boldsymbol{q})$, we have the relation

$$I(\boldsymbol{\kappa}, \tau, \boldsymbol{q}) = F(\boldsymbol{\kappa}, \tau, \boldsymbol{q}+\boldsymbol{\kappa}\tau)\mathrm{e}^{-\tau}$$

Notice that

$$I(\boldsymbol{\kappa}, 0, \boldsymbol{q}) = F(\boldsymbol{\kappa}, 0, \boldsymbol{q})$$

The Fourier transform of the variable $\boldsymbol{s}$ leads to the following differential equation:

$$\frac{\mathrm{d}}{\mathrm{d}\tau}F(\boldsymbol{\kappa}, \tau, \boldsymbol{q}) = p(\boldsymbol{q}-\boldsymbol{\kappa}\tau)F(\boldsymbol{\kappa}, \tau, \boldsymbol{q})$$

The solution is (neglecting reflections at the back wall)

$$\begin{aligned} F(\boldsymbol{\kappa}, \tau, \boldsymbol{q}) &= F(\boldsymbol{\kappa}, 0, \boldsymbol{q})\exp\left\{\int_0^\tau p(\boldsymbol{q}-\boldsymbol{\kappa}\tau')\mathrm{d}\tau'\right\} \\ &= I(\boldsymbol{\kappa}, 0, \boldsymbol{q})\exp\left\{\int_0^\tau p(\boldsymbol{q}-\boldsymbol{\kappa}\tau')\mathrm{d}\tau'\right\} \end{aligned}$$

In fact, the problem is solved for a homogeneous half-space, but a simple model to account for the reflection at the rear end of the cuvette can be included. However, the effect of the reflected wave is small and can be ignored.

To obtain the intensity, the inverse Fourier transforms in the variable $\boldsymbol{\kappa}$ and $\boldsymbol{q}$ are applied. The intensity in the slab at the location $(\boldsymbol{\eta}, \tau)$ in the direction $\boldsymbol{s}$ is

$$\begin{aligned} I(\boldsymbol{\eta}, \tau, \boldsymbol{s}) &= \frac{1}{4\pi^2}\iint_{\mathbb{R}^2} I(\boldsymbol{\kappa}, \tau, \boldsymbol{s})\mathrm{e}^{-\mathrm{i}\boldsymbol{\kappa}\cdot\boldsymbol{\eta}}\,\mathrm{d}\boldsymbol{\kappa} \\ &= \frac{1}{4\pi^2}\iint_{\mathbb{R}^2} F(\boldsymbol{\kappa}, \tau, \boldsymbol{s})\mathrm{e}^{-(1-\mathrm{i}\boldsymbol{s}\boldsymbol{\kappa})\tau-\mathrm{i}\boldsymbol{\kappa}\boldsymbol{\eta}}\,\mathrm{d}\boldsymbol{\kappa} \\ &= \frac{\mathrm{e}^{-\tau}}{16\pi^4}\iint_{\mathbb{R}^2}\iint_{\mathbb{R}^2} I(\boldsymbol{\kappa}, 0, \boldsymbol{q})\mathrm{e}^{-\mathrm{i}(\boldsymbol{\eta}-\boldsymbol{s}\tau)\cdot\boldsymbol{\kappa}-\mathrm{i}\boldsymbol{q}\cdot\boldsymbol{s}} \\ &\quad \exp\left\{\int_0^\tau p(\boldsymbol{q}-\boldsymbol{\kappa}\tau')\mathrm{d}\tau'\right\}\mathrm{d}\boldsymbol{\kappa}\,\mathrm{d}\boldsymbol{q} \end{aligned} \tag{4.1}$$

The exponential containing the phase function $p(\boldsymbol{q})$ models the multiple scattering effects. Without any multiple scattering, $p(\boldsymbol{s}) = 0$, the exponential is replaced with unity, and

$$I(\boldsymbol{\eta}, \tau, \boldsymbol{s}) = I(\boldsymbol{\eta}-\boldsymbol{s}\tau, 0, \boldsymbol{s})\mathrm{e}^{-\tau}$$

which gives the spread and the attenuation of the intensity in the slab.

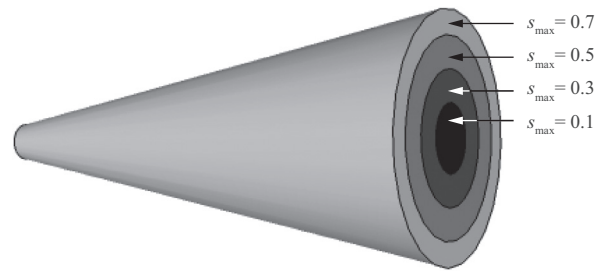

Fig. 7. Graphical illustration of the s_{max} parameter.

The expression in (4.1) models the intensity at the lateral position $\boldsymbol{\eta}$ and depth τ in the direction $\boldsymbol{s}$. At this particular point, the intensity excites the fluorescing dye, which has been added to the mixture to avoid the previously mentioned issues with Mie scattering detection and to improve the accuracy in the measuring process. To model the physics that we expect the SLIPI technique to be governed by, we ignore intensity contributions to the excitation of the fluorescing dye from all directions except for a cone in the forward direction of opening dimension s_{max}, see Fig. 7. Light contributions from other directions are not expected to carry the superimposed line structure used in SLIPI and are therefore removed in the data post-processing. In contrast, all light that maintains a straight path through the sample, despite being scattered on its way, keep the structural imprint and, consequently, are unaffected by the SLIPI filtering.

The average contribution in a cone centered in the forward direction, $\boldsymbol{s} = \boldsymbol{0}$, is

$$I(\boldsymbol{\eta}, \tau, s_{max}) = \frac{1}{\pi s_{max}^2}\iint_{|\boldsymbol{s}|\le s_{max}} I(\boldsymbol{\eta}, \tau, \boldsymbol{s})\mathrm{d}\boldsymbol{s}$$

Notice that we normalize with the area of the domain of averaging πs_{max}^2. This average has only meaning if s_{max} is small, *e.g.*, smaller than the beam width of the phase function $p(\boldsymbol{s})$. The pertinent integral to compute is

$$I = \frac{1}{\pi s_{max}^2}\iint_{|\boldsymbol{s}|\le s_{max}} \mathrm{e}^{-\mathrm{i}(\boldsymbol{q}-\tau\boldsymbol{\kappa})\cdot\boldsymbol{s}}\,\mathrm{d}\boldsymbol{s} = \frac{1}{\pi s_{max}^2}\iint_{|\boldsymbol{s}|\le s_{max}} \mathrm{e}^{-\mathrm{i}\boldsymbol{\xi}\cdot\boldsymbol{s}}\,\mathrm{d}\boldsymbol{s}$$

where $\boldsymbol{\xi} = \boldsymbol{q} - \tau\boldsymbol{\kappa} = \xi(\hat{\boldsymbol{x}}\cos\alpha + \hat{\boldsymbol{y}}\sin\beta)$ and $\boldsymbol{s} = s(\hat{\boldsymbol{x}}\cos\beta + \hat{\boldsymbol{y}}\sin\beta)$ Solve the integral in polar coordinates of $\boldsymbol{s}$, *i.e.*, (s, β).

$$\begin{aligned} I &= \frac{1}{\pi s_{max}^2}\int_0^{2\pi}\int_0^{s_{max}} \mathrm{e}^{-\mathrm{i}\xi s\cos(\beta-\alpha)}s\,\mathrm{d}s\,\mathrm{d}\beta = \frac{2\pi}{\pi s_{max}^2}\int_0^{s_{max}} J_0(\xi s)s\,\mathrm{d}s \\ &= \frac{2}{\xi^2 s_{max}^2}\int_0^{\xi s_{max}} J_0(x)x\,\mathrm{d}x = 2\frac{J_1(\xi s_{max})}{\xi s_{max}} \end{aligned}$$

Notice that if $s_{max} \to 0$, then $I \to 1$.

Finally, the measurements are performed perpendicular to the laser sheet, and the intensity that is recorded by the CCD camera is not only the intensity from a single sphere, but from the entire collecting of spheres along a line η_x = constant and τ = constant. Consequently, the integral of the intensity in the η_y-direction in (4.1) is an accurate model of the intensity recorded, *i.e.*,

$$\langle I(\eta_x, \tau, s_{max})\rangle = \int_{-\infty}^{\infty} I(\boldsymbol{\eta}, \tau, s_{max})\mathrm{d}\eta_y$$

The final expression of the recorded intensity in the cone $|\boldsymbol{s}| \le s_{max}$ collected along the line η_x = constant and τ = constant becomes

$$\langle I(\eta_x, \tau, s_{\max})\rangle = \frac{e^{-\tau}}{4\pi^3}\iint_{\mathbb{R}^2}\int_{-\infty}^{\infty} I(\kappa_x\hat{\boldsymbol{x}}, 0, \boldsymbol{q})\frac{J_1\left(s_{\max}\sqrt{(q_x-\tau\kappa_x)^2+q_y^2}\right)}{s_{\max}\sqrt{(q_x-\tau\kappa_x)^2+q_y^2}}e^{-i\eta_x\kappa_x} \exp\left\{\int_0^\tau p(\boldsymbol{q}-\kappa_x\hat{\boldsymbol{x}}\tau')d\tau'\right\} d\kappa_x\, d\boldsymbol{q} \tag{4.2}$$

This is the final expression of the average intensity in the forward direction in the large scatterers approximation. For a given phase function $p(\boldsymbol{s})$, a three-fold inverse Fourier transform has to be performed to find the average intensity $\langle I(\eta_x, \tau, s_{\max})\rangle$.

4.1. Laser sheet

In this section, we specialize the incident intensity to be of Gaussian form at $\tau = 0$. This particular intensity is relevant for the experiments performed in this paper. Moreover, the phase function is also assumed to have a Gaussian distribution. These approximations are reasonable for the problem under consideration.

The intensity at $\tau = 0$ is assumed to be

$$I(\boldsymbol{\eta}, 0, \boldsymbol{s}) = I_0\sqrt{\frac{8}{\pi^3}}\frac{\nu}{w\sigma_x\sigma_y}e^{-2\eta_y^2/w^2-2s_x^2/\sigma_x^2-2s_y^2/\sigma_y^2}\left(1 + A\cos(\Theta\eta_x+\delta)\right)$$

This is a Gaussian distribution in the η_y direction with beam size $2w$ and angular distribution.[5] The spatial variation in the $\hat{\boldsymbol{x}}$ direction is $1 + A\cos(\Theta\eta_x + \delta)$, and the beam is directed close to the $\hat{\boldsymbol{z}}$ direction. Moreover, $\Theta = 2\pi\nu$ (ν is the spatial frequency in the $\hat{\boldsymbol{x}}$ direction). The intensity contains two spread parameters, σ_x and σ_y, which models the divergence of the light intensity. These parameters avoid a delta distribution in the coherent contribution. This intensity characterizes the laser sheet, radiating in $\hat{\boldsymbol{z}}$, see also [19–21]. These assumptions are motivated by

$$\iint_{\mathbb{R}^2}\int_{-\infty}^{\infty}\left(\int_0^{1/\nu} I(\boldsymbol{\eta}, 0, \boldsymbol{s})d\eta_x\right)d\eta_y\, d\boldsymbol{s} = I_0$$

The constant I_0 is the total incident power flux per period in the x direction.

One critical point in the theory is the approximation of the phase function $p(\boldsymbol{s})$. This function is approximated by a Gaussian function, see Fig. 8.

$$p(\boldsymbol{s}) = \frac{2\alpha}{\pi\beta^2}e^{-2s^2/\beta^2}$$

where β is a measure of the width of the phase function in the forward direction (proportional to λ/D), and α is the single particle albedo. The normalization of the phase function is

$$\iint_\Omega p\, d\Omega \approx \iint_{\mathbb{R}^2} p(\boldsymbol{s})d\boldsymbol{s} = \alpha$$

The average intensity in the forward cone is (details of the derivation are found in Appendix A, see (A.1))

[5] The $1/e^2$ beam width definition is used. If another beam width, say half intensity width $w_{1/2}$, is measured, let $w = w_{1/2}\sqrt{2/\ln 2}$ in the expressions. In the limit of zero beam width, a delta contribution is obtained.

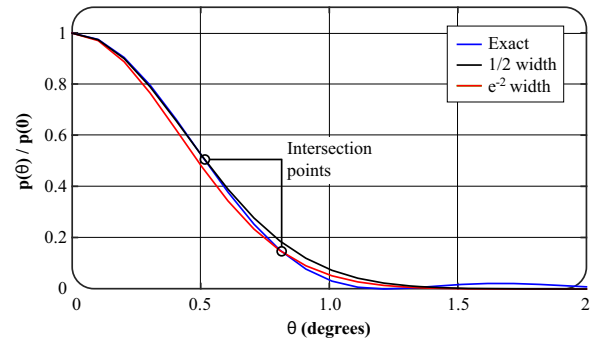

Fig. 8. The normalized phase function $p(\theta)$ for a sphere with diameter $d = 24.90\,\mu$m as a function of the scattering angle θ. A comparison between the numerical (exact) and two approximate computations is depicted.

Table 2
The parameters in the comparison between theory and experiment. The width parameter, w, was set to 50 μm and the modulation depth, A, was set to zero for all simulated cases. The values of $s_{\max}$ are given in percentage of the corresponding width β of the phase function $p(\boldsymbol{s})$ for 25 μm in the forward direction.

No	1	2	3	4	5	6	7	8	9	10
σ_x (mrad)	5	5	10	5	10	5	20	5	40	10
σ_y (mrad)	5	5	5	5	10	1	10	5	10	40
$s_{\max}$ (%)	0	30	10	50	10	70	10	90	10	50

$$\langle I(\eta_x, \tau, s_{\max})\rangle = \frac{\nu I_0}{2\pi^2}e^{-\tau}\iint_{\mathbb{R}^2}\int_{-\infty}^{\infty} e^{-q_x^2\sigma_x^2/8-q_y^2\sigma_y^2/8} \left(\frac{J_1\left(s_{\max}\sqrt{q_x^2+q_y^2}\right)}{s_{\max}\sqrt{q_x^2+q_y^2}}\exp\left\{\alpha\tau e^{-(q_x^2+q_y^2)\beta^2/8}\right\} + A\cos(\Theta\eta_x+\delta)\frac{J_1\left(s_{\max}\sqrt{(q_x-\tau\Theta)^2+q_y^2}\right)}{s_{\max}\sqrt{(q_x-\tau\Theta)^2+q_y^2}} \exp\left\{\alpha e^{-q_y^2\beta^2/8}\int_0^\tau e^{-(q_x-\tau'\Theta)^2\beta^2/8}d\tau'\right\}\right)d\boldsymbol{q}$$

This expression quantifies the average intensity of the laser sheet as a function of the lateral position η_x and depth τ in the cone $s_{\max}$ centered in the forward direction $\boldsymbol{s} = \boldsymbol{0}$.

5. Results

The results of the investigations made in this paper are presented in two subsections. The first subsection collects the results when the modulation depth A is set to zero, *i.e.*, without considering effects introduced by intensity modulation, while the second subsection contains the results when the frequency of the superimposed modulation vary.

5.1. Single frequency

To model the experimental results, the large scatterer approximation was used to solve the RTE.

Comparing simulations and experiments requires exact knowledge of β, $s_{\max}$, σ_x, and σ_y, which are difficult to assess experimentally with adequate accuracy. Ten different simulations were therefore performed, each having a different set of input parameters, permitting us to find the settings which best agreed — qualitatively — with our SLIPI results. Note, however, that the

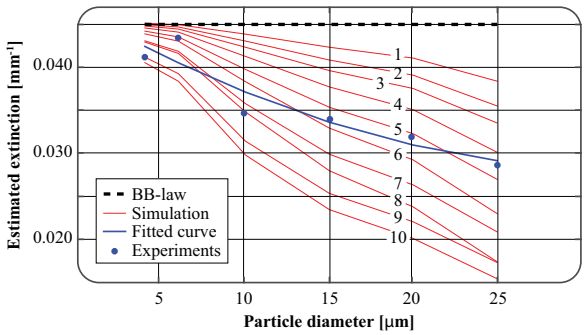

Fig. 9. Comparison between the experiments and the ten simulated cases (each marked with its case number). To quantify the agreement, the extinction of light is estimated (in mm^{-1}). The extinction is estimated for $17 < z < 37$ mm, *i.e.*, in the center of the cuvette.

aim of the current study is not achieving absolute agreement between experiments and simulations — this would require a more rigorous optical setup — but rather capturing and explaining the trends previously observed with SLIPI. The explicit values of the input parameters for the ten cases are given in Table 2.

Fig. 9 displays the agreement between the SLIPI experiments and the ten simulated cases, compared by estimating the extinction of light along the z direction. The fitting routine employed here is based on a single exponential intensity decay. Although deviations between experiments and simulations are observed, both show a similar trend – as the particle size increases, the extinction reduces. Note that this is not in agreement with the Bouguer-Beer law, which predicts a constant extinction of $0.045\ \text{mm}^{-1}$ for all particle sizes (dashed line). We consider the ability to reproduce this somewhat contradicting trend as a validation of the fidelity of our theoretical model and we now study its implications on extinction measurements in more detail.

Our computations verify that the observed reduced extinction of light intensity couples to an increased forward-scattering for larger scatterers as was suggested by Kristensson et al. [8]. However, the model also reveals that additional factors will affect experimental attempts to measure the extinction of light caused by scattering, namely, the spread of the laser sheet along the x and y direction (σ_x and σ_y, respectively) as well as the permitted "forward cone", $s_{\max}$, see Fig. 7. This "forward cone" is added to the model to better simulate a typical imaging measurement situation, which has a finite (pixel-based) sampling. The influence of all these factors on the extinction of light can be seen in Fig. 10, showing experimental decay curves as well as simulations for five different cases.

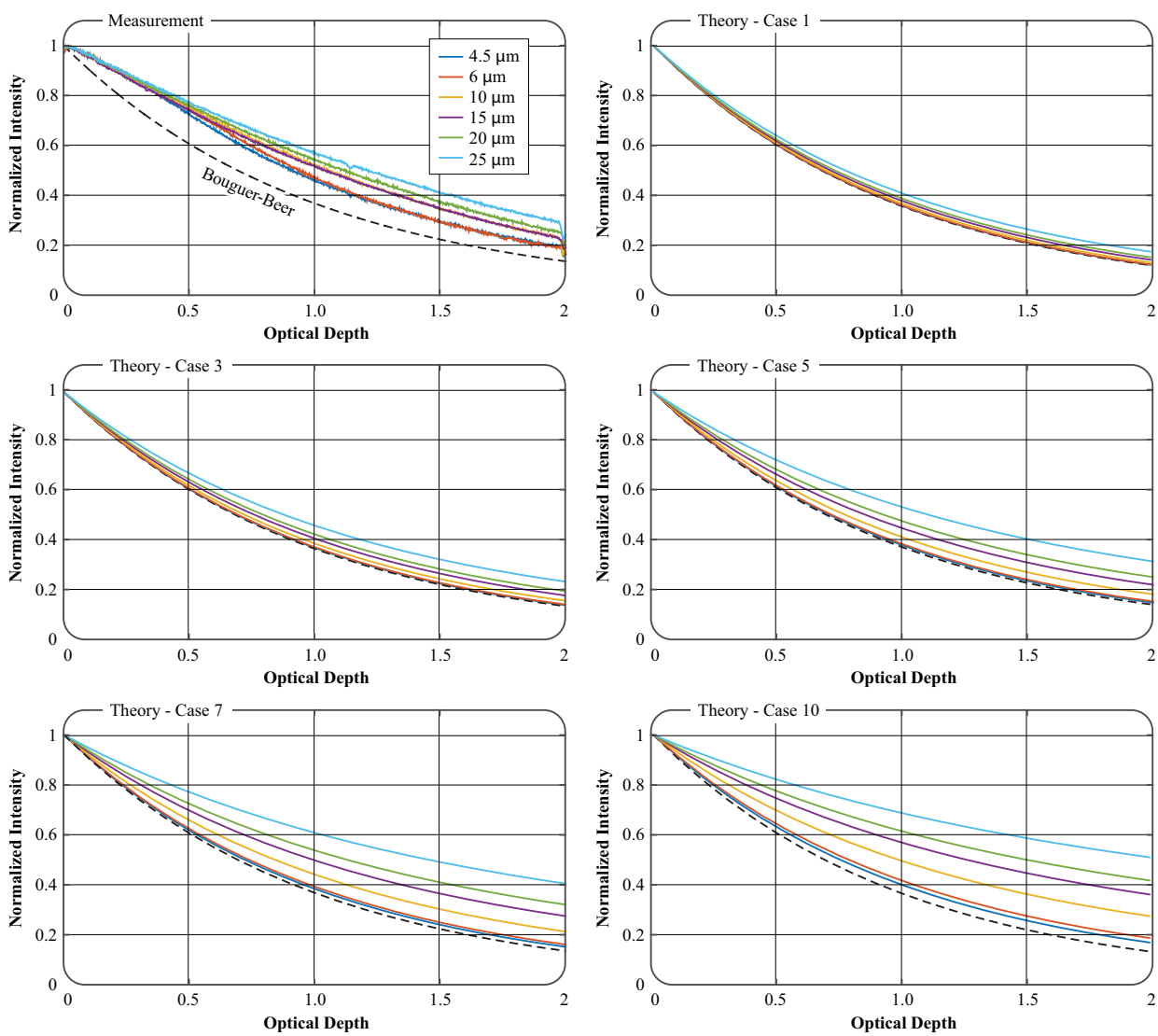

Fig. 10. Results from experiments and five of the simulations, showing the local light intensity as a function of optical depth. The trend observed in the SLIPI data is clearly captured by the model, which further predicts significant deviations from the Bouguer-Beer law as the spread parameters vary.

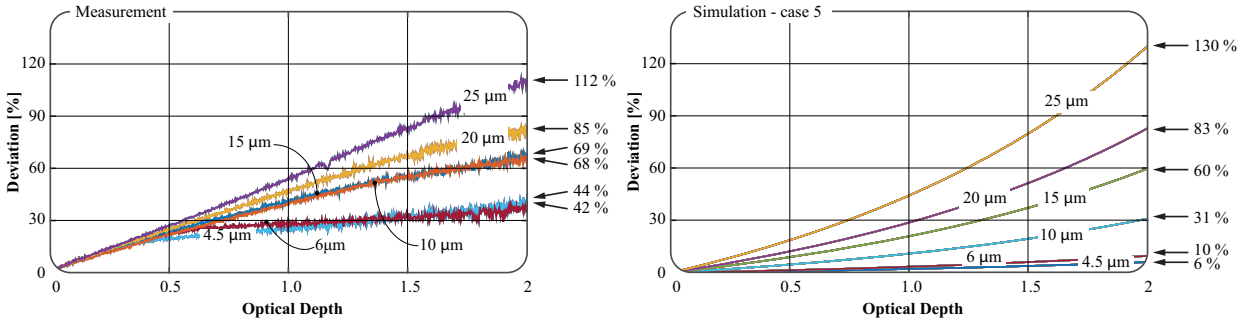

Fig. 11. Deviations between the Bouguer-Beer law and the attenuation predicted by our model, given in percentage. The curves show that measurements performed on smaller particles agree better with the Bouguer-Beer law whereas measurements performed on larger particles give a significantly reduced extinction.

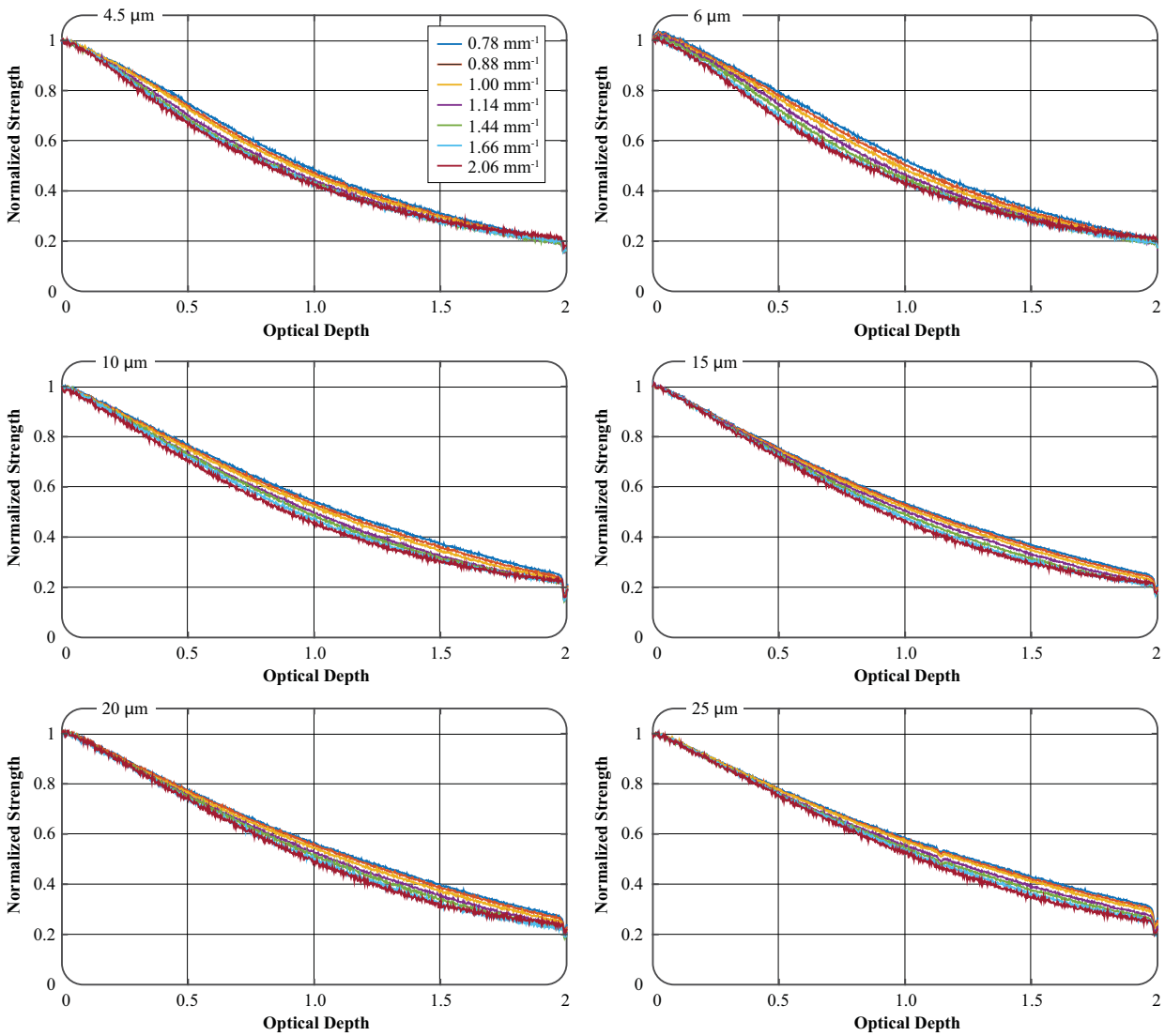

Fig. 12. Results from SLIPI experiments performed with seven different spatial frequencies, demonstrating that an increased modulation frequency leads to results that are in better agreement with the Bouguer-Beer law.

Case 1 in Fig. 10 is considered an ideal measurement situation, having a laser sheet with a very low divergence in both spatial directions and a "perfect" detector with $s_{\max} = 0$. The simulations still show a spread in the decay curves, *i.e.*, larger particles extinct light less effectively, yet the effect is not too pronounced and would probably be regarded as a measurement error if observed experimentally. Case 3 is a more realistic situation, where both the spreading of the laser sheet along the x and y direction are slightly increased and the finite sampling of the detector is considered ($s_{\max}$ = 10% of the width β of the phase function $p(\boldsymbol{s})$ for 25 µm in

the forward direction). The effect seen in case 1 has now increased, showing a 68% higher intensity at $\tau = 2$ for the largest particles (25 μm) compared to the smallest one (4.5 μm). The "extreme" case — case 10 — displays strong deviations from the Bouguer-Beer law and the difference in the reduction of light intensity is clearly observable. In this simulation, the intensity at $\tau = 2$ is nearly 200% higher for 25 μm compared to 4.5 μm — a deviation that is unlikely to be dismissed as a measurement error.

From the results shown in Figs. 9 and 10, it becomes clear that forward-scattering (*i.e.*, the β term) is not solely responsible for the observed deviations from the Bouguer-Beer law. Experimental factors such as the divergence of the laser sheet and the finite sampling of the full system are also important and will affect the outcome of a measurement. Fig. 11 quantifies the observed deviation from the Bouguer-Beer law for the measurement data as well as for simulation case 5. A maximum deviation of 112% is observed for the former case, while the corresponding value for the simulation is slightly higher (130%).

5.2. Variable frequency

Thus far, the spatial frequency of the superimposed modulation has not been considered. To investigate the influence of this parameter, seven SLIPI measurements (Fig. 12) were performed where the spatial frequency of the intensity modulated laser sheet was varied, see values in Table 3.

Fig. 12 shows normalized attenuation curves (1D cross sections) of the SLIPI results for the different spatial frequencies and for all particle sizes. While the influence of the spatial frequency is not too apparent for small particles, it becomes more noticeable for the larger ones. For 25 μm, the effect is strongest, and the acquired data reveals that as the spatial frequency increases, the light appears to be attenuated more rapidly with distance, *i.e.*, a characterized by a higher extinction. Note that this trend cannot be explained by uncertainties associates with the preparation of the samples, as all different frequency measurements are acquired from the same sample. This trend can partly be understood from a sampling point-of-view; SLIPI can only reject the intensity contribution from multiply scattered light, if the light appears to be originating from a "dark" fringe (see example in Fig. 13). Scattering occurring along the incident trajectory cannot be distinguished from the unperturbed light, which lead to the trends discussed in Section 5.1. However, there is most likely a certain "degree of freedom" for the light, which we model by the parameter $s_{\max}$. If the off-axis scattering is only minute and light intensity diverts only a fraction of a degree from the forward direction — often referred to as "snake photons" [22] — SLIPI will fail to identify and reject the corresponding intensity contribution as it would appear to be originating from a "bright" fringe. Such a "degree of freedom" should thus be coupled with (1) the modulation frequency and (2) the sampling of the data. Fig. 13 illustrates this for two laser sheets having different modulation frequencies, observed with a camera with a given resolution (shown as a grid). When the frequency is low (left case), forward scattered light is more likely to be unnoticed by SLIPI, even if the events would result in a shift in the row of pixels — the "degree of freedom" is relatively large. The opposite is expected to occur for finer modulation patterns (right case). In this case, off-axis scattering can only be unnoticed if the event occurs within a narrow forward cone, *i.e.*, a small value of $s_{\max}$.

However, the above explanation would apply for all particle sizes, yet the effect that higher spatial frequencies lead to a gradually increased extinction is more pronounced for larger particles. Fig. 14 illustrates this size-dependency, showing the estimated extinction coefficient for each particle size as a function of spatial frequency. The calculations are based on the same approach as for the results in Fig. 9. The extracted values of the extinction coefficient show a clear trend — small particles are much less effected by the spatial frequency of the superimposed intensity modulation than the larger particles. We attribute this size-dependency once again to differences in the scattering phase function. To explain, consider the extreme case of purely isotropic scattering. The effects observed and described in Section 5.1 — the preservation of intensity in the forward direction due to a pronounced forward scattering lobe — is in this case negligible. Consequently, reducing the "degree of freedom" by increasing the spatial modulation frequency of SLIPI would thus have an insignificant impact on the end result. However, when the light intensity is concentrated in the forward direction, the amount of

Table 3
The spatial frequencies of the superimposed intensity modulation used to investigate the influence of this parameter.

Case	1	2	3	4	5	6	7
$\nu(\mathrm{mm}^{-1})$	0.784	0.879	0.995	1.145	1.437	1.657	2.063

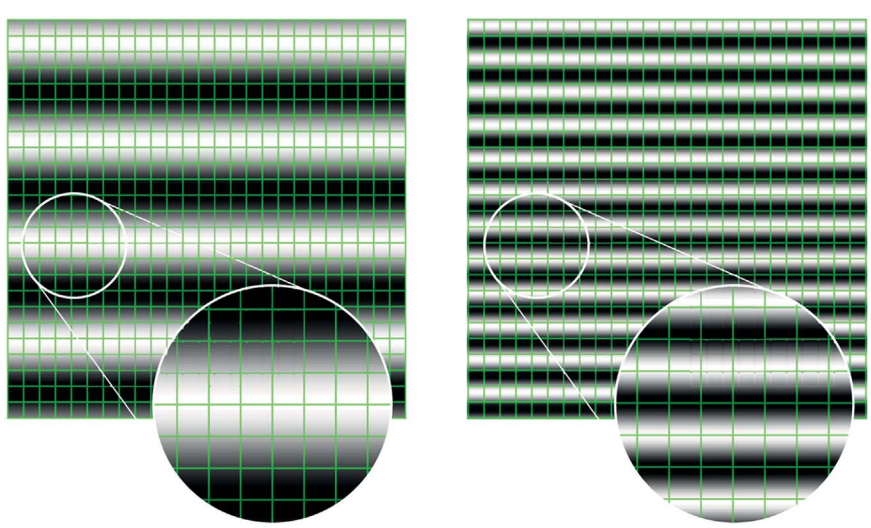

Fig. 13. Illustration of the influence of a finite sampling and modulation frequency of the SLIPI laser sheet. When the modulation frequency is low (left), light can be slightly scattered off-axis without SLIPI being able to detect it. However, when the superimposed modulation patter is finer (right), the risk for such events to go unnoticed is reduced and the performance of SLIPI is expected to be improved.

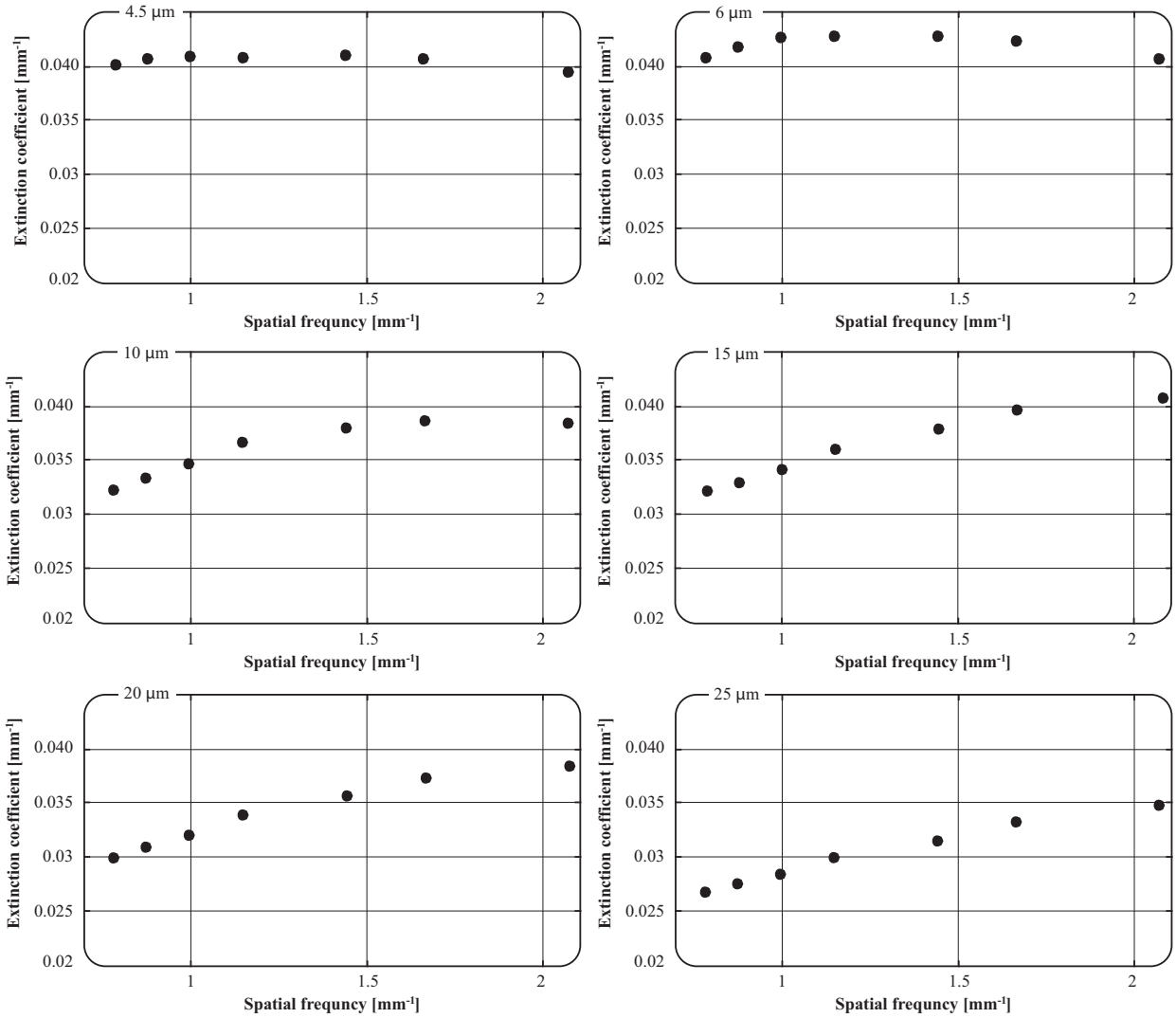

Fig. 14. The evaluated extinction coefficient for the measurement cases presented in Fig. 12. The data shows that the frequency of the superimposed intensity modulation mostly affects measurements performed on relatively larger particles.

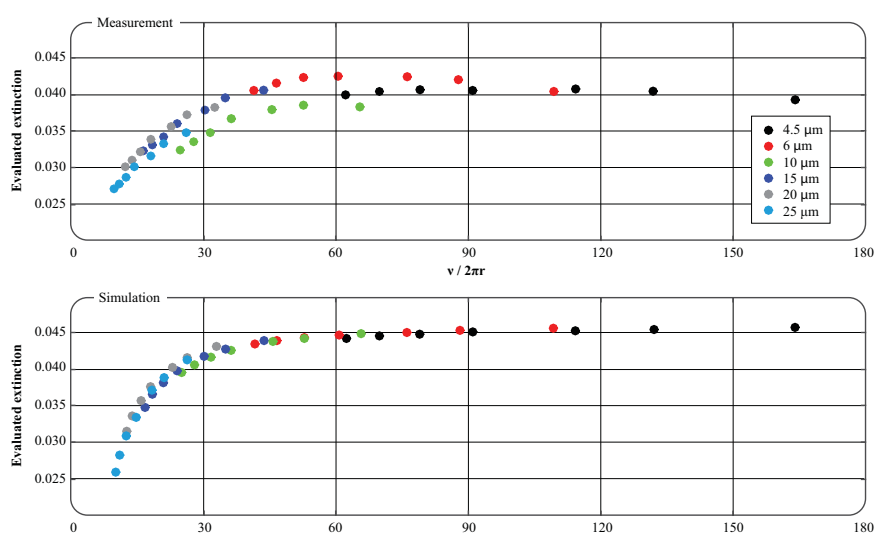

Fig. 15. The extinction coefficient data in Fig. 14, plotted as a function of $\nu/2\pi r$. The graphs reveal an interesting trend, SLIPI measurements performed on different particle sizes appear to have an inherent interconnected behavior. Small values of $\nu/2\pi r$ under-predicts the extinction coefficient. As $\nu/2\pi r$ increases, by either increasing ν or decreasing the diameter of the scatterer, the estimated extinction coefficient approaches the "correct" value, to finally flatten out and stagnate. The lower graph is a model prediction of this behavior and is in good agreement with the measurement (upper graph).

"snake photons" increases and the medium falsely appears less turbid. By gradually improving the filtering capacity of SLIPI by increasing the spatial modulation frequency, more and more "snake photons" will fall within a "dark" fringe and, consequently, be removed in the data post-processing. Hence, the more pronounced the forward scattering lobe is, the more the influence of a reduction of the "degree of freedom".

Fig. 14 shows that the evaluated extinction coefficient gradually increases for larger particles as the modulation frequency becomes finer while for smaller particles it stagnates at $\approx 0.043\ \mathrm{mm}^{-1}$, never fully reaching the expected value of $0.045\ \mathrm{mm}^{-1}$ as predicted by the Bouguer-Beer law. However, if these extinction coefficient data points are plotted together they reveal an interesting trend, see Fig. 15. In this graph, the extinction coefficient values are plotted as a function of $\nu/2\pi r$, where r is the radius of the particles in mm. This normalization is applied to compensate for the difference in modulation frequency experienced by the different particles — a given modulation pattern appears finer for larger particles. However, when normalized in this fashion, the acquired data shows that there is a clear link between modulation frequency and particle size. Specifically, the data shows that regardless of the particle size, a SLIPI measurement performed with a relatively low modulation frequency gives results that deviates from the Bouguer-Beer law or, equivalently, the sample appears less turbid. As the spatial frequency is increased, the result approaches the Bouguer-Beer law prediction. Although the physical interpretation of this relationship is not investigated in further detail, we note that it has one important consequence; according to the results in Fig. 15, different particles respond differently as the modulation frequency is altered and quantifying this response could potentially be a measurement approach to assess particle size. We aim to investigate this discovery and its practical aspects in more detail in a companion paper.

6. Discussion and conclusions

In summary, we have conducted SLIPI measurements in several turbid ($OD=2$), scattering environments of mono-disperse particle distributions with known concentrations. SLIPI was employed to suppress interference caused by multiply scattered light that otherwise make imaging in such turbid situations difficult, permitting us to visualize the local extinction of light from the side. A theoretical model was developed that calculates the attenuation of light intensity through the laser sheet. The model uses the large scatterer approximation to solve the Radiative Transfer Equation, yet it has additional constrains to best model the SLIPI process. Light that diverges from its initial trajectory during the propagation through the sample is suppressed by the SLIPI technique. However, should the initial trajectory be maintained as light scatters upon the spherical, non-absorbing particles, its intensity is unaffected. This effect, which influences other measurement techniques as well, was included in the model (see (4.2)).

The experiments and the theoretical predictions are in good agreement, both clearly showing how the current conception of light extinction — the Bouguer-Beer law — is not completely accurate in these turbid environments from an experimental perspective. For example, the model shows that the measurable opacity of a homogeneous sample with particles of 25 μm in diameter with the current optical arrangement is reduced by roughly 130% at an (expected) optical depth of 2 — a deviation that should be considered in quantitative measurements that are based on light attenuation caused partly or entirely by scattering. The deviation from the Bouguer-Beer law is illustrated in Fig. 11. However, our study demonstrates how the deviation from this law can be quantified, potentially opening up for a new strategy to determine particle size.

We have summarized the main discoveries of the current study below:

- Probing turbid, scattering samples having different mono-disperse particle sizes but (theoretically) equal opacities leads to measurable differences in terms of light extinction.
- For a given *OD*, samples with larger particles appear less opaque, *i.e.*, they transmit more light. This, in turn, is beneficial in terms of visualization, yet may render difficulties making quantitative assessments.
- The Bouguer-Beer law in its current form does not take the preservation of the energy in the forward direction into account. Experimentally, unperturbed and forward-scattered light can be very difficult (if possible) to differentiate.
- Light energy being preserved in the forward direction is not a unique concern for SLIPI measurements, but should be classified as a *general* light-matter interaction feature, affecting, in principle, all light-based probing techniques employed in scattering environments.
- The finite sampling of the detector as well as the spread of the laser sheet (or beam) affects the magnitude of the deviations from the Bouguer-Beer law.
- The performance of SLIPI depends on the spatial frequency of the superimposed modulation, where a finer pattern yields results that are in better agreement with the Bouguer-Beer law.
- The impact of the spatial frequency of the superimposed intensity modulation depends on the size of the probed particles — the larger, the more the effect is pronounced.
- By probing a sample with different modulation frequencies and quantifying the change in response could open up for a new means to measure particle size.

To the best of our knowledge, the trends presented in this study have not been observed in the past, which we believe is due to two factors. First, the deviation from the Bouguer-Beer law is not observed at low optical depths, and imaging through/in turbid media is associated with a great experimental difficulty. Only a few optical methods with this capacity do exist, SLIPI being one of them. Ballistic imaging [22], which is used both for tissue imaging and for spray visualization, has the capability of visualizing through strongly scattering media, yet provides "only" line-of-sight information. Since the effects discovered in this study are occurring locally within the sample, they are unlikely to be observed with line-of-sight techniques. Second, measurements based on side-scattering detection of light in scattering environments are often deteriorated by out-of-plane contributions stemming from multiple light scattering. The effects discovered in this study are probably too minute in comparison to have been observed using such conventional techniques.

Despite a generally good agreement between experiments and our theoretical model, there are, however, several sources of error that should be addressed. First, since the particle number density varied between samples, so did the accuracy on the concentration. However, we find it extremely unlikely that this would generate the trends observed herein. Second, unlike simulations, experimental measurements face obstacles such as a limited dynamic range, vignetting, detector noise, laser power fluctuations, *etc.* that affects the fidelity of the measurements. Third, the exact optical parameters — especially σ_x, σ_y and $s_{\max}$ — could not be established with sufficient accuracy with the current setup. Due to these reasons, achieving an exact agreement between simulations and the results obtained experimentally have not been the main focus of this study, but rather to investigate whether the trends observed in the laboratory could be understood and explained theoretically.

Acknowledgements

The first author (EK) would like to show his appreciation to the Swedish Research Council (grant number 121892).

Appendix A. Laser sheet (Gaussian shape)

This appendix contains the details of the computations of the intensity for an incident intensity at $\tau = 0$ of Gaussian form. Moreover, the phase function is also assumed to have a Gaussian distribution. These approximations are reasonable for the problem under consideration.

Assume the intensity at $\tau = 0$ has a Gaussian distribution in the η_y direction with beam width size $2w$ and a $1 + A\cos(\Theta\eta_x + \delta)$ variation in the vertical η_x direction. The explicit form is

$$I(\boldsymbol{\eta}, 0, \boldsymbol{s}) = I_0\sqrt{\frac{8}{\pi^3}}\frac{\nu}{w\sigma_x\sigma_y}\mathrm{e}^{-2\eta_y^2/w^2-2s_x^2/\sigma_x^2-2s_y^2/\sigma_y^2}\big(1 + A\cos(\Theta\eta_x + \delta)\big)$$

where $\Theta = 2\pi\nu$ (ν is the spatial frequency in the $\hat{\boldsymbol{x}}$ direction). This incident intensity models the laser sheet relevant for present experiments. The intensity contains two spread parameters, σ_x and σ_y, which models the divergence of the light intensity.

The Fourier transform of the intensity at $\tau = 0$ is

$$\begin{aligned} I(\boldsymbol{\kappa}, 0, \boldsymbol{q}) &= \iint_{\mathbb{R}^2}\iint_{\mathbb{R}^2} I(\boldsymbol{\eta}, 0, \boldsymbol{s})\mathrm{e}^{\mathrm{i}\boldsymbol{\kappa}\cdot\boldsymbol{\eta}+\mathrm{i}\boldsymbol{q}\cdot\boldsymbol{s}}\,\mathrm{d}\boldsymbol{\eta}\,\mathrm{d}\boldsymbol{s} \\ &= 2\pi\nu I_0\mathrm{e}^{-\kappa_y^2w^2/8-q_x^2\sigma_x^2/8-q_y^2\sigma_y^2/8} \\ &\quad\left(\delta(\kappa_x) + \frac{A}{2}\big(\delta(\kappa_x + \Theta)\mathrm{e}^{\mathrm{i}\delta} + \delta(\kappa_x - \Theta)\mathrm{e}^{-\mathrm{i}\delta}\big)\right) \end{aligned}$$

In particular,

$$\begin{aligned} &I(\kappa_x\hat{\boldsymbol{x}}, 0, \boldsymbol{q}) \\ &\quad = 2\pi\nu I_0\mathrm{e}^{-q_x^2\sigma_x^2/8-q_y^2\sigma_y^2/8}\left(\delta(\kappa_x) + \frac{A}{2}\big(\delta(\kappa_x + \Theta)\mathrm{e}^{\mathrm{i}\delta} + \delta(\kappa_x - \Theta)\mathrm{e}^{-\mathrm{i}\delta}\big)\right) \end{aligned}$$

The phase function is approximated as ($s = \sqrt{s_x^2 + s_y^2}$)

$$p(\boldsymbol{s}) = \frac{2\alpha}{\pi\beta^2}\mathrm{e}^{-2s^2/\beta^2}$$

where β is a measure of the width of the phase function in the forward direction (proportional to λ/D), and α is the single particle albedo. The normalization is

$$\iint_\Omega p\,\mathrm{d}\Omega \approx \iint_{\mathbb{R}^2} p(\boldsymbol{s})\mathrm{d}\boldsymbol{s} = \alpha$$

The Fourier transform of the phase function is ($q = \sqrt{q_x^2 + q_y^2}$)

$$p(\boldsymbol{q}) = \frac{2\alpha}{\pi\beta^2}\iint_{\mathbb{R}^2}\mathrm{e}^{-2s^2/\beta^2+\mathrm{i}\boldsymbol{q}\cdot\boldsymbol{s}}\,\mathrm{d}\boldsymbol{s} = \alpha\mathrm{e}^{-q^2\beta^2/8}$$

The average intensity in the forward direction, see (4.2), is

$$\begin{aligned} &\big\langle I(\eta_x, \tau, s_{\max})\big\rangle \\ &\quad = \frac{\mathrm{e}^{-\tau}}{4\pi^3}\iint_{\mathbb{R}^2}\int_{-\infty}^{\infty} I(\kappa_x\hat{\boldsymbol{x}}, 0, \boldsymbol{q})\frac{J_1\left(s_{\max}\sqrt{(q_x - \tau\kappa_x)^2 + q_y^2}\right)}{s_{\max}\sqrt{(q_x - \tau\kappa_x)^2 + q_y^2}}\mathrm{e}^{-\mathrm{i}\eta_x\kappa_x} \\ &\qquad \exp\left\{\int_0^\tau p(\boldsymbol{q} - \tau'\kappa_x\hat{\boldsymbol{x}})\mathrm{d}\tau'\right\}\mathrm{d}\kappa_x\,\mathrm{d}\boldsymbol{q} \end{aligned}$$

Introduce the Fourier transformed intensity at $\tau = 0$ and the Fourier transform of the phase function.

$$\begin{aligned} &\big\langle I(\eta_x, \tau, s_{\max})\big\rangle \\ &\quad = \frac{\nu I_0}{2\pi^2}\mathrm{e}^{-\tau}\iint_{\mathbb{R}^2}\int_{-\infty}^{\infty}\mathrm{e}^{-q_x^2\sigma_x^2/8-q_y^2\sigma_y^2/8}\frac{J_1\left(s_{\max}\sqrt{(q_x - \tau\kappa_x)^2 + q_y^2}\right)}{s_{\max}\sqrt{(q_x - \tau\kappa_x)^2 + q_y^2}} \\ &\qquad \left(\delta(\kappa_x) + \frac{A}{2}\big(\delta(\kappa_x + \Theta)\mathrm{e}^{\mathrm{i}\delta} + \delta(\kappa_x - \Theta)\mathrm{e}^{-\mathrm{i}\delta}\big)\right)\mathrm{e}^{-\mathrm{i}\eta_x\kappa_x} \\ &\qquad \exp\left\{\alpha\mathrm{e}^{-q_y^2\beta^2/8}\int_0^\tau \mathrm{e}^{-(q_x-\tau'\kappa_x)^2\beta^2/8}\,\mathrm{d}\tau'\right\}\mathrm{d}\kappa_x\,\mathrm{d}\boldsymbol{q} \end{aligned}$$

The κ_x integration is readily evaluated.

$$\begin{aligned} \big\langle I(\eta_x, \tau, s_{\max})\big\rangle &= \frac{\nu I_0}{2\pi^2}\mathrm{e}^{-\tau}\iint_{\mathbb{R}^2}\mathrm{e}^{-q_x^2\sigma_x^2/8-q_y^2\sigma_y^2/8} \\ &\quad\left(\frac{J_1\left(s_{\max}\sqrt{q_x^2 + q_y^2}\right)}{s_{\max}\sqrt{q_x^2 + q_y^2}}\exp\left\{\alpha\tau\mathrm{e}^{-(q_x^2+q_y^2)\beta^2/8}\right\}\right. \\ &\quad + A\cos(\Theta\eta_x + \delta)\frac{J_1\left(s_{\max}\sqrt{(q_x - \tau\Theta)^2 + q_y^2}\right)}{s_{\max}\sqrt{(q_x - \tau\Theta)^2 + q_y^2}} \\ &\quad\left.\exp\left\{\alpha\mathrm{e}^{-q_y^2\beta^2/8}\int_0^\tau \mathrm{e}^{-(q_x-\tau'\Theta)^2\beta^2/8}\,\mathrm{d}\tau'\right\}\right)\mathrm{d}\boldsymbol{q} \end{aligned} \tag{A.1}$$

The integral inside the exponential can be computed in terms of the error function $\mathrm{Erf}(z)$

$$\int_0^\tau \mathrm{e}^{-(q_x-\Theta\tau')^2\beta^2/8}\,\mathrm{d}\tau' = \frac{\sqrt{2\pi}}{\beta\Theta}\left(\mathrm{Erf}\left[\frac{\beta q_x}{2\sqrt{2}}\right] - \mathrm{Erf}\left[\frac{\beta((q_x - \tau\Theta))}{2\sqrt{2}}\right]\right)$$

References

[1] Berrocal E, Kristensson E, Richter M, Linne M, Aldén M. Application of structured illumination for multiple scattering suppression in planar laser imaging of dense sprays. Opt Express 2008;16:17870–17881.
[2] Kristensson E, Berrocal E, Aldén M. Two-pulse structured illumination imaging. Opt Lett 2014;39:2584–2587.
[3] Dyer MJ, Crosley DR. Two-dimensional imaging of oh laser-induced fluorescence in a flame. Opt Lett 1982;7:382–384.
[4] Neil R, Juskaitis MAA, Wilson T. Method of obtaining optical sectioning by using structured light in a conventional microscope. Opt Lett 1997;22:1905–1907.
[5] Keller PJ, Stelzer EH. Quantitative in vivo imaging of entire embryos with digital scanned laser light sheet fluorescence microscopy. Curr Opin Neurobiol 2008;18:624–632.
[6] Adrian R. Twenty years of particle image velocimetry. Exp Fluids 2005;39:159–169.
[7] Kristensson E, Ehn A, Bood J, Aldén M. Advancements in rayleigh scattering thermometry by means of structured illumination. In: Proceedings of the 35th International symposium on combustion; 2015. p. 3689–96.
[8] Kristensson E, Araneo L, Berrocal E, Manin J, Richter M, Aldén M, Linne M. Analysis of multiple scattering suppression using structured laser illumination planar imaging in scattering and fluorescing media. Opt Express 2011;19:13647–13663.
[9] Bouguer P. Essai d'optique; 1729.
[10] Mishchenko MI. Directional radiometry and radiative transfer:the convoluted path from centuries-old phenomenology to physical optics. J Quant Spectrosc Radiat Transf 2014;146:4–33 [Electromagnetic and Light Scattering by Nonspherical Particles {XIV}].
[11] Ma X, Lu JQ, Brock RS, Jacobs KM, Yang P, Hu X-H. Determination of complex refractive index of polystyrene microspheres from 370 to 1610 nm. Phys Med Biol 2003;48:4165.
[12] Chandrasekhar S. Radiative transfer.New York: Dover Publications; 1960.
[13] Ishimaru A. Wave propagation and scattering in random media.Single scattering and transport theory, 1. New York: Academic Press; 1978.
[14] Mishchenko MI, Travis LD, Lacis AA. Multiple scattering of light by particles: radiative transfer and coherent backscattering.Cambridge, UK: Cambridge University Press; 2006.
[15] Cheung RL-T, Ishimaru A. Transmission, backscattering, and depolarization of waves in randomly distributed spherical particles. Appl Opt 1982;21:3792–3798.
[16] Gabriel P, Tsay S, Stephens G. A Fourier-Riccati approach to radiative transfer. Part I: foundations. J Atmos Sci 1993;50:3125–3147.
[17] Kristensson G. Scattering of electromagnetic waves by obstacles.Edison, NJ,

USA: SciTech Publishing; 2016.
[18] Ishimaru A. Theory and application of wave propagation and scattering in random media. Proc IEEE 1977;65:1030–1061.
[19] Deepak A, Farrukh UO, Zardecki A. Significance of higher-order multiple scattering for laser beam propagation through hazes, fogs, and clouds. Appl Opt 1982;21:439–447.
[20] Tam WG, Zardecki A. Laser beam propagation in particulate media. JOSA 1979;69:68–70.
[21] Fante R. Propagation of electromagnetic waves through turbulent plasma using transport theory. IEEE Trans Antennas Propag 1973;21:750–755.
[22] Linne M, Paciaroni M, Berrocal E, Sedarsky D. Ballistic imaging of liquid breakup processes in dense sprays. Proc Comb Inst 2009;32:2147–2161.